Final Report

Experimental Equipment for Powder Processing

Contract Number FA9550-06-1-0417

Patrick Kwon

Department of Mechanical Engineering

Michigan State University

East Lansing, Michigan 48824

pkwon@egr.msu.edu

(517) 355-0173

Report Documentation Page		*Form Approved* *OMB No. 0704-0188*

1. REPORT DATE **20 AUG 2009**	2. REPORT TYPE **Final**	3. DATES COVERED **01-06-2006 to 31-12-2008**

4. TITLE AND SUBTITLE **Experimental Equipment for Powder Processing**	5a. CONTRACT NUMBER **FA9550-06-1-0417**
	5b. GRANT NUMBER
	5c. PROGRAM ELEMENT NUMBER
6. AUTHOR(S) **Patrick Kwon**	5d. PROJECT NUMBER
	5e. TASK NUMBER
	5f. WORK UNIT NUMBER

7. PERFORMING ORGANIZATION NAME(S) AND ADDRESS(ES) **Department of Mechanical Engineering,Michigan State University,East Lansing,MI, 48824**	8. PERFORMING ORGANIZATION REPORT NUMBER **; AFRL-OSR-VA-TR-2011-0238**

9. SPONSORING/MONITORING AGENCY NAME(S) AND ADDRESS(ES) **Byung-Lip Lee, 875 North Randolph Street, Suite 325, Arlington, VA, 22203**	10. SPONSOR/MONITOR'S ACRONYM(S)
	11. SPONSOR/MONITOR'S REPORT NUMBER(S) **AFRL-OSR-VA-TR-2011-0238**

12. DISTRIBUTION/AVAILABILITY STATEMENT
Approved for public release; distribution unlimited

13. SUPPLEMENTARY NOTES

14. ABSTRACT
MTS Insight systems are ideal for performing standard tests such as peel, tear, sheer, tensile, compression, and flex/bend [4]. MTS Insight 300 offers high-capacity testing capabilities up to 300 kN. As shown in Fig.2, it features a floor-standing frame made for high-capacity strength tests such as tensile, compression, and characterization of higher-force materials. The motion of the crosshead is controlled by code TestWorks? Testing Software. Offering user-defined crosshead speeds as well as advanced control modes such as load and strain, MTS Insight 300 can analyze material properties of larger specimens. Common applications include metals, ceramics, high-strength components, large fasteners, structural materials, and composite materials. Operators can easily run tests, review results, and report and archive data with the flexible and user friendly TestWorks? Testing Software.

15. SUBJECT TERMS
peel, tear, sheer, tensile, sheer, flex, fasteners, structural, materials and Test Works

16. SECURITY CLASSIFICATION OF:			17. LIMITATION OF ABSTRACT	18. NUMBER OF PAGES	19a. NAME OF RESPONSIBLE PERSON
a. REPORT **unclassified**	b. ABSTRACT **unclassified**	c. THIS PAGE **unclassified**	**Same as Report (SAR)**	**24**	

1. Reasons

To increasing the safety factor of the space vehicles, Perspirable Skin, a new designed Thermal Protection System (TPS) was proposed by bio-mimicking the process of human sweating. Perspirable Skin is arranged in a 'Peg and Hole' fashion, as shown in Fig. 1. The RCC panels are with numerous holes, in which cores (pegs) made of another material are assembled. The core material has smaller Coefficient of Thermal Expansion (CTE) that RCC. As temperature increases, a gap is produced between the RCC skin and cores due the CTE difference. Once the temperature reaches the working temperature, a compressed gas contained in tank inside the space vehicle blow out from the gap. The cold gas flows over the surface and mixes with the atmospheric air to compensate the frictional heat between the vehicle and the atmospheric air, keeping the surface at a lower temperature than that of present TPS. After the vehicles landed and its surface temperature decreases, the gap closes again.
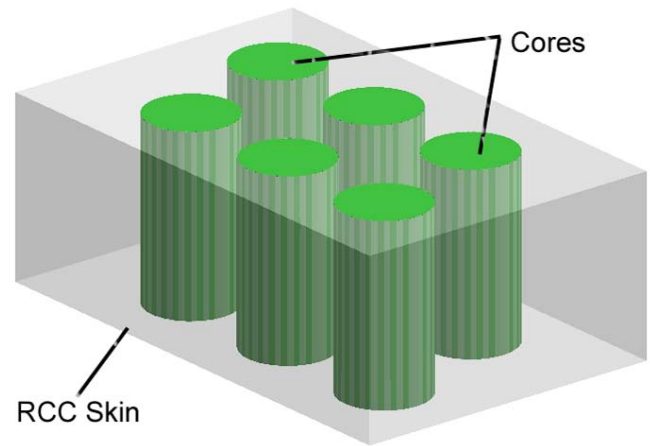

Fig.1 Schematics of Perspirable Skin TPS

Due to the high temperature working condition and low CTE requirement, ceramic is the best candidate materials to manufacturing the core of Perspirable Skin. Powder Metallurgy (P/M) is the study of the processing of powders. It is the most common fabrication method for most ceramic and some metal engineering components [1]. Compared to most other processing methods, P/M is cheaper. Therefore, P/M was considered to be the best candidate method to fabricate core materials for Perspirable Skin.

The three main steps of P/M to convert powders into useful objects are 1) powder processing, 2) forming operations, and 3) sintering [1]. The powder processing may involve milling and mixing [2]. Many methods are being used in forming operations of powders such as injection molding, slurry techniques and compaction [1]. Conventional uniaxial powder compaction, which is performed with the pressure applied along one axis using hard tooling of die and punches, is the most widely used method to compact powders. Samples after compaction are called "greens", which are the precursor for attaining a dense body by sintering. Sintering describes the formation of bonds between particles close to their melting point. It can occur at temperatures below the melting point by solid-state atomic transport phenomenon. However, some instances involve the formation of a liquid phase [1, 3]. On a microstructural scale, the bonding occurs as cohesive necks grow at the particle contacts [1-3].

To perform the compaction and sintering as well as monitor the sintering kinetics/densification in the sintering, a Material Test System, MTS Insight 300 (MTS Systems Corp. USA) and a Thermomechanical Analysor (TMA), SETARAM SETSYS Evoluation 95 (SETARAM instrumentation, France), were procured.

2. MTS Insight 300

2.1 Introduction

MTS Insight systems are ideal for performing standard tests such as peel, tear, sheer, tensile, compression, and flex/bend [4]. MTS Insight 300 offers high-capacity testing capabilities up to 300 kN. As shown in Fig.2, it features a floor-standing frame made for high-capacity strength tests such as tensile, compression, and characterization of higher-force materials. The motion of the crosshead is controlled by code TestWorks™ Testing Software. Offering user-defined crosshead speeds as well as advanced control modes

Fig.2 MTS Insight 300 system

such as load and strain, MTS Insight 300 can analyze material properties of larger specimens. Common applications include metals, ceramics, high-strength components, large fasteners, structural materials, and composite materials. Operators can easily run tests, review results, and report and archive data with the flexible and user friendly TestWorks™ Testing Software. Table 1 shows some product specifications of MTS Insight 300.

Table 1. Product Specifications of MTS Insight 300 [4]

Force Capacity	300 kN	Crosshead Travel Space	1150 mm
Weight	1050 kg	Height x Width x Depth	2440 x 1133 x 685 mm^3
Frame Stiffness	300 kN	Maximum Test Speed	500 mm/min
Power	6.0 kW	Speed Accuracy	± 0.05% of full speed
Maximum Test Speed	500 mm/min	Position Accuracy	0.01 mm
Minimum Test Speed	0.001 mm/min	Position Resolution	0.001 mm
Motor and Drive System		AC Brushless, 3 ph sinusoidal	

2.2 Application in Perspirable Skin project

MTS Insight 300 is used to compact various ceramic powders to forming green samples. Fig.3 shows the positions of cross heads and the uniaxiadie set in the compaction process. The detailed compaction process is shown in Fig. 4. The loose, free flowing powder is introduced into the die cavity in the filling step. The upper surface of the powder was flattened. Then the top punch is forced into the die to compact the powder. After compaction, the relative density of compact is around 50% for most ceramic powders. In the ejection step, the forces acting upon the punches are removed and the top punch is used to eject the sample from the confines of the die.
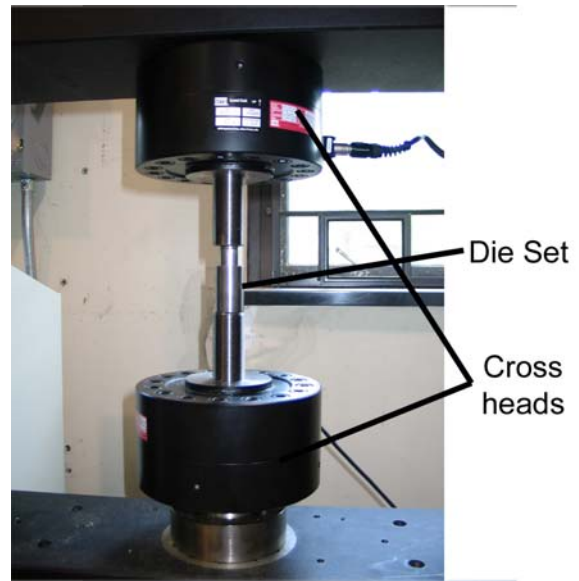

Fig.3 The assembly of die set in the MTS Insight 300

Except fabricating green samples, MTS Insight 300 was also used to 1) investigate the Powder mixing effect on the compaction capabilities of ceramic powders; 2) determine the mechanical properties of greens; and 3) investigate the density distribution inside a green compact.
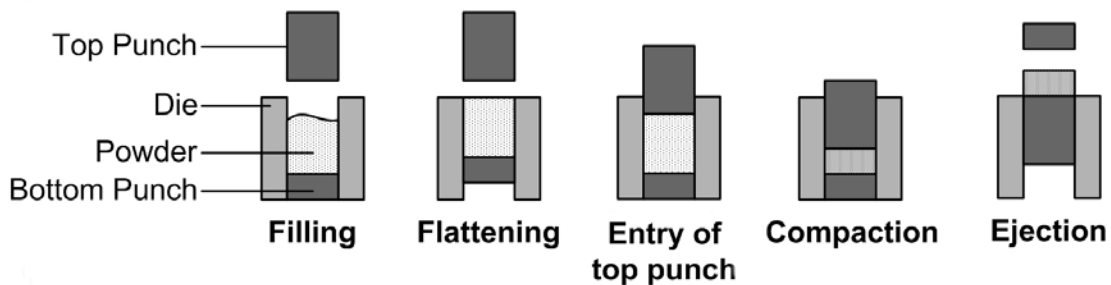

Fig.4 The process of die set compaction.

2.3 Representative experimental results

2.3.1 Powder mixing effect on the compaction capabilities of ceramic powders [5]

In the compaction experiments, by recording the force, displacement, stress and strain, MTS Insight 300 can provide us the relative density-stress curves or relative density-strain curves. Those curves were compared in order to investigate the powder mixing effect on the compaction capabilities of ceramic powders [5].

In the series of experiments, four high-pure and undoped alumina (Al_2O_3) powders with submicron/micron particle sizes were investigated. The four powders were TMDAR

(Taimei Chemical CO., LTD., Japan), CR-15, CR-6, and GE-1 (Baikowski Ind. Corp., U.S.A.). All possible two-powder combinations with the four powders were mixed in various mass ratios, and in total six powder mixture systems were produced. The mixture systems include TMDAR+CR-15, TMDAR+CR-6, TMDAR+GE-1, CR-15+CR-6, CR-15+GE-1, and CR-6+GE-1. In addition to four unmixed powders, each system contains nine powder mixtures, in which the proportions of one powder in the mixtures range between 10% and 90% in 10% intervals. In total, fifty-four powder mixtures were studied. Six grams of each powder mixture poured into a single-action die made of 1144 Stress Proof steel. The inner diameter of the die, D_{in}, is 22.19mm. Before pouring the powders into the die, the die wall was lubricated with graphite powder (Panef Corp., USA).

The top surface of the powder was flattened and then the top punch was inserted into the die until it touched the powder. The compaction load was applied on the top punch by MTS Insight 300. The speed was 10mm/min and the stress resolution is 0.013MPa. During the compaction, only the top punch moved. The compressive forces applied on the top (F_t) and bottom punches (F_b) as well as the displacement of the top punch (Z_t) were recorded continuously as a function of time by the load sensors. At first, the pre-load of 0.5MPa was applied to set an initial state. The preload is necessary to measure the compact characteristics accurately before starting the main compacting process. After pre-loading, the initial height of each sample, h_i, was measured. This was done by measuring the total height of the two punches and the pre-loaded compact inside the die, then subtracting the height of the two punches. Considering the diameter of each compact to be the same as the inner diameter of the die, D_{in}, the initial relative density, R_i, can be calculated by the following equation:

$$R_i = \frac{\rho_i}{\rho_f} = \frac{m/V_i}{\rho_f} = \frac{m}{\dfrac{3.975}{4}\pi D_{in}{}^2 h_i} \qquad (1)$$

where m, V, and ρ represent mass, volume, and density, respectively, and the subscripts i and f represent initial and theoretically fully value. The theoretical fully-density of alumina was taken as 3.975g/cm^3.

After obtaining the initial relative density, the die set with pre-loaded compact was put back into the load frame, and then the load of 80MPa was applied to compact samples. The final green samples produced a diameter of 22.19mm and their heights ranged from 7.05mm to 9.1mm. Several green samples were coated with nail polish and then their volumes were measured in water by Archimedes' principle. Those values were then compared to the corresponding volumes calculated by the final sample heights, h_f, and diameter, D_{in}. The discrepancies between the two groups of values were minimial, less than 1.1%. Therefore, only the calculated volumes were used to calculate the densities.

By the recorded top punch displacement, Z_t, and the initial compact height, h_i, or final

compact height, h_f, the sample height, h_t, at time t can be calculate,

$$\begin{cases} h_t = h_i - Z_t & \text{(2.a)} \\ h_t = h_f + Z_t & \text{(2.b)} \end{cases}$$

The h_t calculated by Eq. (2.a) and (2.b) for any compact was the same. Therefore, two separate measurements, h_i and h_f, for each compact were for self-consistency.

From the calculated h_t, similar to calculating the initial relative density, the relative density at time t, defined as R_t, can be found as,

$$R_t = \frac{\rho_t}{\rho_f} = \frac{m/V_t}{\rho_f} = \frac{m}{\dfrac{3.975}{4}\pi D_{in}{}^2 h_t} \qquad (3)$$

In Eq. (3), the sample diameter was assumed to be matching the inner diameter of the die, D_{in}.

The corresponding stress, σ_t, at time t can be obtained by the punch diameter, D_{in}, and the recorded load, F_t.

$$\sigma_t = \frac{F_t}{S_t} = \frac{F_t}{\dfrac{1}{4}\pi D_{in}{}^2} \qquad (4)$$

where S_t is the cross-sectional area of the top punch.

The relative density-stress curves for each powder mixture group were then drawn. Fig. 5.a and Fig. 5.b show the representative curves for the TMDAR+CR-15 and CR-6+GE-1 powder mixture groups, respectively. For clarity, only six curves were included in each figure.
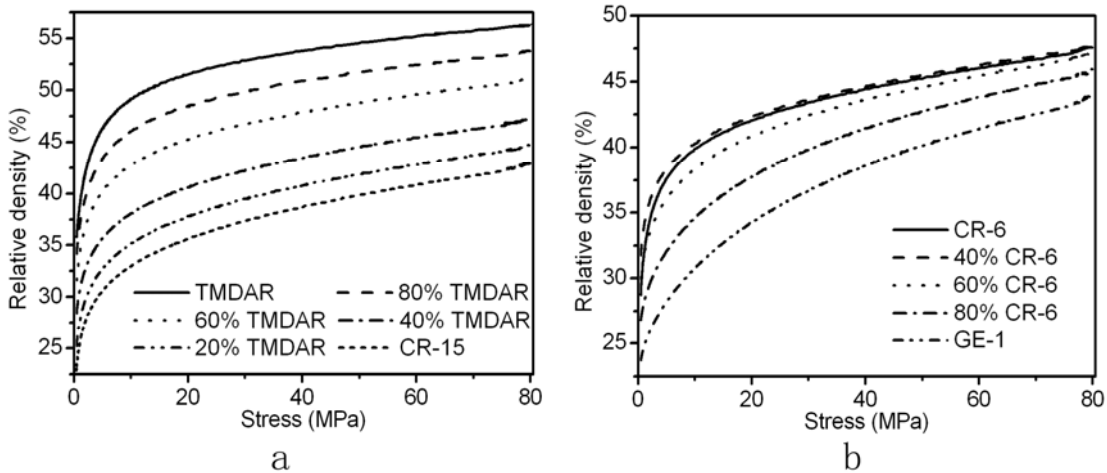

Fig.5 The relative density-stress curves by the compaction for a) CR-15+TMDAR and b) CR-6+GE-1 [5].

Under a constant compaction load or stress, the difference of the relative densities represents the change in the compaction capability in different mixtures. A higher relative

density represents improved compaction capability. Even the absolute relative density values continuously increase with the increase in the compaction load, the relationship between the relative density and powder proportions remains similar for each powder mixture group as observed in Fig. 5. Therefore, one can conclude that the starting powder combination determines the compaction capability of each powder mixture. In addition, the initial relative densities dictated by the starting powder combination can be used to quantify and compare the compaction capability of each powder mixture.

The relationships between the initial relative density and the powder proportion are shown in Fig.6 for all six powder mixture groups. For each curve, the left end is the 100% of the fine powder and the right end is the 100% of the coarse powder. The "fine" or "coarse" powder is defined by the average particle size $\bar{D}$ of the powder.
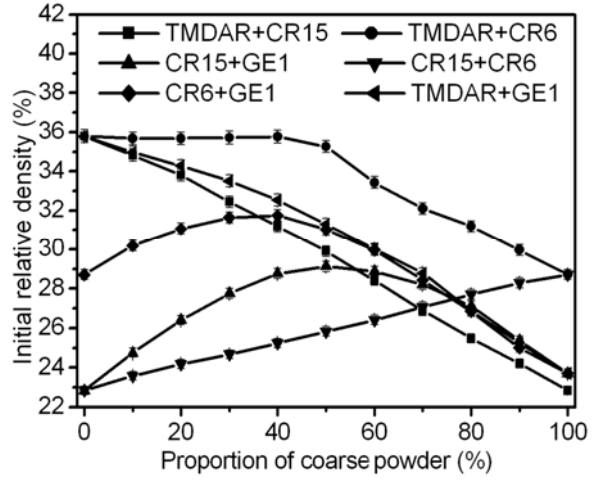

Fig.6 The initial relative density – coarse powder proportion for all six powder mixture groups after 0.5MPa pre-load compaction [5].

$$\bar{D}_{GE-1} > \bar{D}_{CR-6} > \bar{D}_{CR-15} > \bar{D}_{TMDAR} \qquad (5)$$

Fig. 6 shows two kinds of relationships between the initial relative density and the proportion of the coarse powder.

1. Linear relationship: TMDAR+CR-15 and CR-15+CR-6 powder mixture groups show this characteristic. The maximum relative density corresponds to 100% of one of the powders.

2. Nearly parabolic relationship: The maximum relative density of some powder groups with this relationship occurs with certain powder mixtures, such as TMDAR+CR-6, CR-15+GE-1, and CR-6+GE-1. This is similar to the conclusion of Westman [6] and McGeary [7]. However, the proportions of coarse powder in the powder mixture that attained the maximum relative density are between 40% and 60%. These values differ from the reported 30% by Westman [6] and McGeary [7] for sand and metal balls. Another powder systems, TMDAR+GE-1, has the maximum relative density at 100% TMDAR.

In the study of ceramic powders' compaction, Aydin *et al.* [8-10] defined axial true strain $\bar{\varepsilon}_t$ as the following,

$$\bar{\varepsilon}_t = \left| \ln\left(\frac{h_t}{h_i}\right) \right| \qquad (6)$$

Fig. 7(a) and Fig. 7(b) show the representative relative density-strain curves for the TMDAR+CR-15 and CR-6+GE-1 powder mixture groups, respectively. Comparing Fig. 7 and Fig. 5, the powder mixture with better compaction capability/density in Fig. 5 is also with a higher relative density under any strain values in Fig. 7.
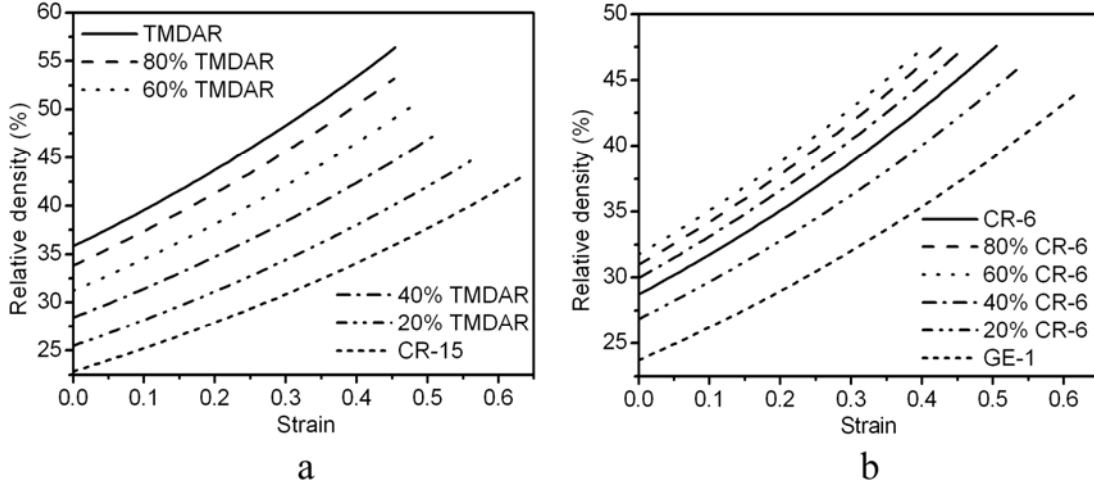

Fig.7 The relative density-strain curves by the compaction for a) CR-15+TMDAR and b) CR-6+GE-1 [5].

The Mircocal Origin and Wolfram Mathematica software were employed to calculate the trend functions of the relative density-strain curves. The relationship exactly fits into the following equation for each powder mixture,

$$R_t = \kappa e^{\bar{\varepsilon}t} \qquad (7)$$

where k has the same unit as density, g/cm^3. Table 2 displays several k value for the TMDAR+CR-15 powder mixture group.

Table 2　The coefficient k in Equation (3.7) for representative TMDAR+CR-15 powder mixture

CR-15	0%	10%	50%	70%	90%	100%
(g/cm^3)	1.4228	1.3843	1.1887	1.0688	0.9622	0.908

Eq. (7) shows that a powder mixture with a higher density/compaction capability has a larger k value. Compared the k values in Table 2 to the corresponding initial relative density value in Fig.6, they are the same. This indicates the physical meaning of k in Eq. (7) is the "initial relative density". From the relative density and strain definitions in Eq. (3) and (6) as well as Eq. (1), the conclusion can be verified.

Therefore, the method to compare compaction capability of various powder mixtures from their relative density-strain curves only needs to consider the initial relative density value. In other words, from either the relative density-stress or the relative density-strain

curves, one can use Fig. 6 to find the difference in the compaction capabilities of powder mixtures.

By further analysis, we found the shape of the initial relative density versus proportion of coarse powder curve depends on the ratio of average particle size, and the difference in the initial density of two powders. If the average particle size ratio is less than 3.6, or the average particle size ratio is larger than 3.6 but the initial relative density different is higher than 10%, the curve is linear. If the average particle size ratio is larger than 3.6 and the initial relative density difference is smaller than 10%, the curve is parabolic. The triangle enclosed by the line intersecting the relative density of the fine powder and the maximum relative density of the coarse powder, the line intersecting the relative density of the coarse powder and the maximum relative density of the fine powder as well as the line connecting the relative density of the fine and coarse powder form the boundary of the initial relative density-proportion of coarse powder curve, as shown in Fig.8 [5].
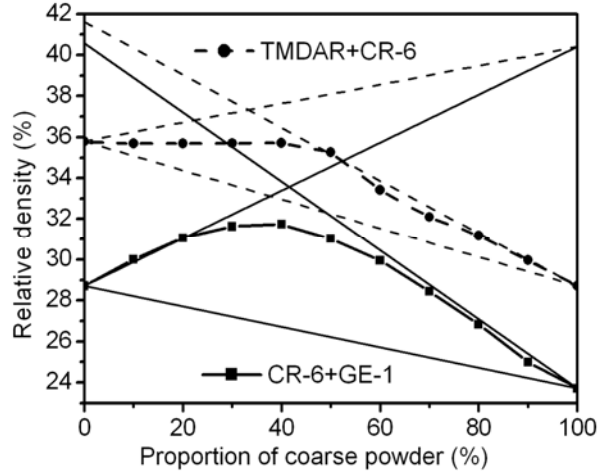
Fig.8 Triangle boundaries for the initial relative density-coarse powder proportion curves of TMDAR+CR-6, CR-6+GE-1 powder groups [5].

2.3.2 Determination of the mechanical properties of greens

The stress-strain relationship in both loading and unloading parts can be recorded by MTS Insight 300, as shown in Fig.9. The elastic unloading part of the stress-strain curves for the powders is linear. The slope of the elastic unloading part (m), the bulk modulus (K), the shear modulus (G), the Young's modulus (E) and the Poisson's ratio (υ) have relationship as listed in Eqs. 8-10 [11].
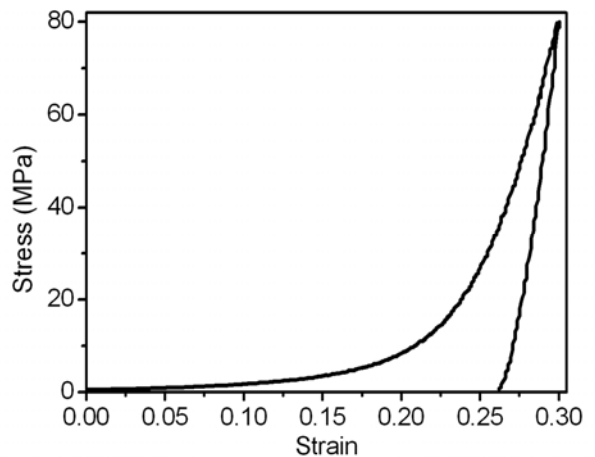
Fig.9 Stress-strain curve of TMDAR in both loading and unloading parts

$$m = K + \frac{4}{3}G \qquad (8)$$

$$E = \frac{9GK}{3K+G} \qquad (9)$$

9

$$v = \frac{3K - 2G}{2(3K + G)} \qquad (10)$$

The TMA unit offers a facility to measure Young's modulus of materials (E) using the three-point bending method, which will be discussed in Section////. The Young's modulus of CR-15 compact by 80MPa is 1031.3 MPa, and that of TMDAR is 2155 MPa. Therefore, by measured Young's modulus and the calculated slope value, the other moduli and Poisson's ratio can be obtained, as listed in Table 3.

Table 3 Material properties for several alumina compacts

Powder	TMDAR	CR-15
Young's modulus (MPa)	2155.1	1031.3
Unloading slope (MPa)	2498.3	1250.4
Shear modulus (MPa)	876.1	410.8
Bulk modulus (MPa)	1329.9	702.3
Poisson's ratio	0.23	0.255

2.3.3 Density distribution inside green compacts

The densities of a green compact are not even everywhere, but with a density distribution [8, 9]. We used colored powder as tracer to investigate the density distribution insider green compacts.

In Section 2.3.1, we already discovered that powder mixing changes the compaction capability. Therefore, we dyed several powder mixtures by stamp-ink (2000 plus, Red, COSCO, Germany). The mixtures then were put into a furnace (Carbolite-HTF1700, UK) for 4 hours at 70°C to dry out. The remained solids were put into bottles with 12mm diameter alumina mixing media. The bottles were on a jar mill (U.S. Stoneware 764AVM, U.S.A.) for 48 hours to break the solids. Then the powders were sifted to get colored powder with size less than 0.3mm.

The colored powders were compacted to 0.5MPa to get the initial densities as mentioned in Section 2.3.1. Then the values were compared with five different main powder (mixture): TMDAR, 50/50 TMDAR/CR15, CR15, 50/50 CR15/GE1, and GE1, respectively. The colored powder with same compaction capability to a powder (mixture) will be used as its compaction indicator.

To investigate the density distribution insider a green compact, the height of the green sample cannot be two small. Otherwise, the density distribution will be in a small range, hard to identify. So in this study, we keep the height/diameter ratio of each green sample around 1.1-1.2. The diameter of the samples is 19.04 mm. In the experiments, we kept the thickness of each main powder layer are identical, also each colored powder layer. And the thickness of colored powder layer is around 1/15 of the main powder layer. Based on these requirements, the powder mass of each layer can be calculated. The main powder is 1.5g for each layer and the colored powder mass is between 0.12g for

each layer.

Similar to the compaction procedure in Section 2.3.1, the first layer powder, which always is main powder, was pour into the die, which was lubricated with graphite powder (Panef Corp., USA). Then a pre-load of 0.5MPa was applied to compact the first layer to obtain enough stiffness. After the pre-compaction, the die set was moved from the MTS Insight 300. The layer thickness, measured by subtracting he height of the two punches form the total height of the two punches and the pre-loaded compact inside the die, was recorded. The top punch was then dragged out of the die slowly and then the second layer powder (colored powder) was pour into the die. Flatting the surface of the new layer powder and putting the top punch back to the die, the 0.5 MPa pre-load was applied on the both layer again. Repeat the procedure till the last layer was pre-loaded. Finally the load of 80MPa was applied to compact the whole multi-layered samples.

The green samples were then took out the die and polished carefully on the lateral surface till to the middle section. Then each sample was placed on a sample holder for photo taking. The photos were took by a dissection microscope (Wild M5A, Wild Heerbrugg Ltd, Switzerland). The representative picture of the middle section is shown in Fig.10. Due to the axial symmetric characteristics of the density distribution in the compact, the broken parts in the left edge shown in Fig.10 do not influence the calculation of the density distribution contour.
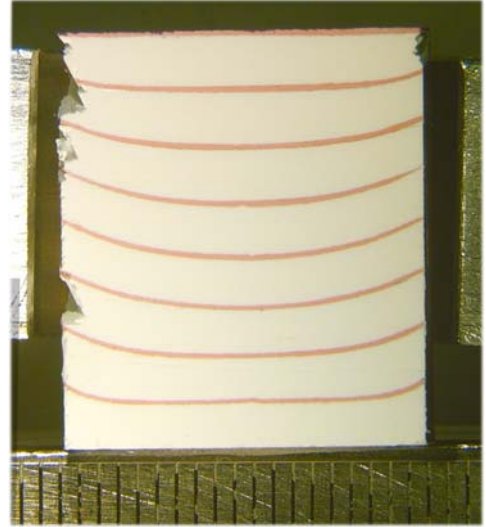
Fig.10 The photo of the middle section of a TMDAR sample. The bottom side in the picture is also the side contact to the bottom punch in the compaction.

Based on Eqs 6 and 7, the relative density ρ_t can be calculated as:

$$\rho_t = \rho_i e^{\left|\ln\left(\frac{ht}{hi}\right)\right|} \qquad (11)$$

where ρ_i is the initial density after 0.5MPa, which already is presented in Fig.6 for each main powder. The final height of a position, h_t, is obtained by analyzing the photo by software Image G. Since each indicator layer is curved after compaction as shown in Fig.10, the h_t varies by positions. Therefore, different position is with different density.

The density distribution contour was plotted by MatLab, Fig.11 shows the contour of TMDAR, in which the 0 position is corresponding to the center axial in the Fig.10. All other four powder compacts feature similar density distribution contour as shown in Fig.11. But the density distribution range varies as different powders as listed in Table 4. Similar to the average density relationship in Fig.6, powders with better compaction capability have both larger lowest density and highest density. From Fig. 11, one can see that the high-density regions exist at the near the bottom central region and on the central

axis. And the low-density regions are at the bottom edges and near the top center. Our results are similar to Aydin et al [8, 9] and others' report [13-15].
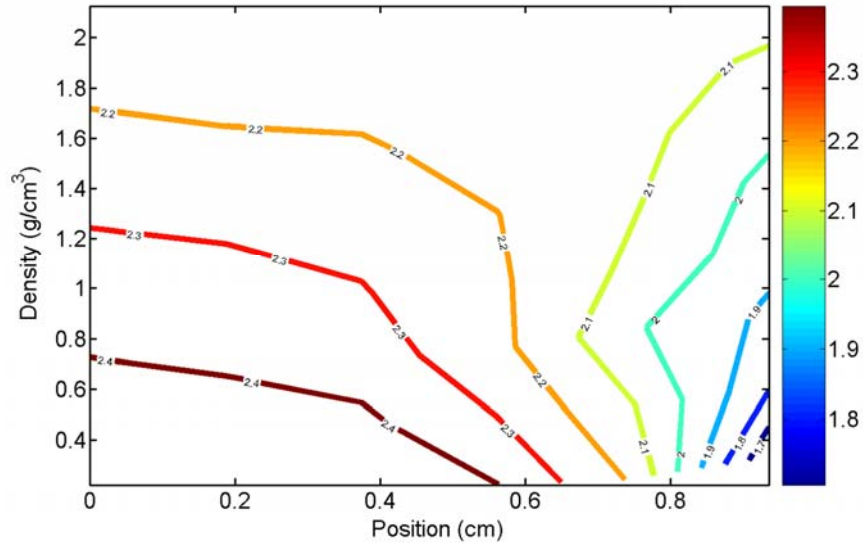

Fig.11 The density distribution of TMDAR green sample, zero position is the radial symmetric axel in Fig.10.

Table 4 The lowest and highest density in various samples

Powder	Lowest density (g/cm^3)	Highest density (g/cm^3)
TMDAR	1.618	2.462
CR-15	1.199	1.662
GE-1	1.203	1.671
50/50 TMDAR/CR15	1.409	2.064
50/50 CR15/GE1	1.414	1.867

3. TMA - SETARAM SETSYS Evoluation 95

3.1 Introduction

SETARAM SETSYS Evoluation 95 is designed by SETARAM instrumentation, France (http://www.setaram.com/). This machine measures the deformation of a sample under non-oscillating stress against time or temperature with prescribed ramp/soak path. The testing temperature range of SETSYS Evolution 95 is from room temperature to 1750°C [16]. Fig.12 shows the front view of this analyzer.

When the head cover open, the sample can be put in sample chamber, which is an alumina tube. A probe connecting to a displacement transducer is arranged in the sample chamber. The position of the probe can be adjusted so its tip can touch the top surface of

the sample, as shown in Fig.13. For the sintering kinetics and CTE test, a 5-gram load is applied to the probe to ensure the contact with a sample throughout the entire experiment. It has been verified that this small force does not influence the testing results [17]. For the Young's modulus measurement, the force can be as large as 200 grams. The displacement transducer equipped in the SETSYS Evolution 95 is characterized by its robustness and high accuracy; it can detect dimension changes as small as 0.01 micron. The transducer uses an electromagnetic system for automatic control of the force applied to the sample, between 0.01 and 1.5 N. The force can be increased by adding weights (up to 200 grams) on a top plate. Transducer calibration and force control are managed automatically by computer [16].

Fig.12. The front view of the SETARAM SETSYS Evoluation 95 (1-head cover, 2-furnace side watch, 3-mode changing switch, 4-open/close head switch, 5-side cover, 6-proctective gas inlet and outlet tube).

The SETSYS Evoluation 95 has a cylindrical furnace. The heating element is made up of graphite rube and fitted in the centerline of the furnace. The thermocouple is composed of Pt/Pt-Rh and can withstand temperatures as high as $1750^{\circ}C$ [16].

3.2 Application in Perspirable Skin project

Except as a regular furnace to sinter samples with oxidization-protection environment, with its software, the SETSYS Evolution 95 can be used as a dilatometer to test many material properties, such as the thermal expansion coefficients (CTE), the softening temperature, the glass transition point and so on. The SETSYS Evolution 95 is also particularly suitable for measuring controlled-rate sintering. By measuring the displacement of one dimension and performing calculations, this TMA can give the shrinkage rate–sintering temperature curve or densification rate–relative density curve. By a specially designed probe and support, the SETSYS Evolution 95 also can perform 3-point flexure measurements, which would give the temperature dependence of the Young's modulus of the testing material.
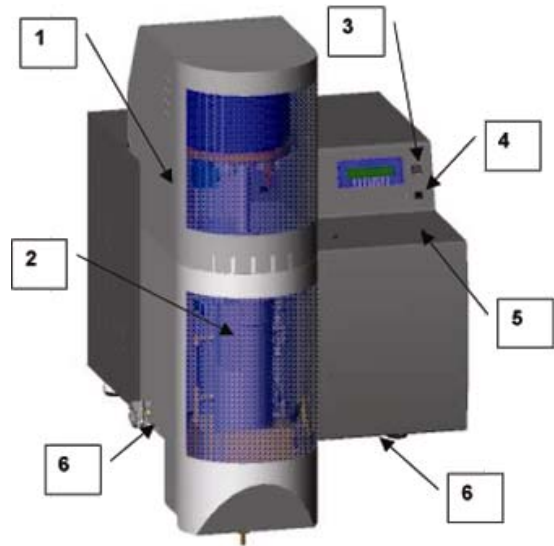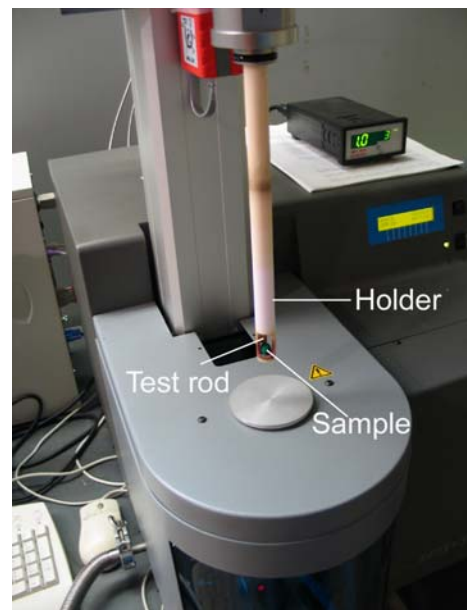

Fig.13 Sample position inside the TMA

3.3 Representative experimental results

3.3.1 Sintering kinetics curves [18, 19]

Two types of curves are commonly used to describe the sintering kinetics: the shrinkage rate–sintering temperature curve and the densification rate–relative density curve. For the latter one, the relative density D is the ratio of the mass density of the sample to the theoretical density of the corresponding powder mixture. And the densification rate is defined as:

$$\dot{\varepsilon}^s(T) = \frac{\partial \rho}{\rho \partial t} = \frac{\dot{D}(T)}{D(T)} \qquad (12)$$

We investigated the sintering kinetics for a series of alumina and zirconia powder mixtures by TMDAR, CR-15 (alumina), as well as TZ3YS and CERAC-2003 (zirconia). The proportion of TMDAR in alumina system and CERAC-2003 in zirconia system ranges from 0% to 100% in 10% intervals, resulting in a total of 22 powder mixture samples in this study.

From the TMA testing results, we calculated and plotted densification rate-relative density curves to describe the sintering kinetics of each powder mixture. Since the TMA can measure the length change in only one direction, to calculate the densification rate based on the results of TMA, Lance et al. [20] defined an anisotropic shrinkage factor α:

$$\alpha = \frac{(\varphi_f - \varphi_O)L_O}{(L_f - L_O)\varphi_O} \qquad (13)$$

where Lo and Lf are the initial and final height of the specimen, and φo and φf are the initial and final mean diameters of a specimen. For each of our experimental results, α was almost 1 (>0.991). It is therefore reasonable to consider the sintering process for our samples to be a self-similar (isotropic) one. Thus, with the 1:1 height to diameter ratio, the temperature dependent relative density can be calculated from the following expression:

$$D(T) = \left[\frac{1 + \dfrac{L_f - L_O}{L_O}}{1 + \dfrac{\Delta L(T)}{L_O}} \right]^3 D_f = \left[\frac{L_f}{L_O + \Delta L(T)} \right]^3 D_f \qquad (14)$$

where Df is the relative density of the fully-sintered sample, $\triangle L(T)$ is the displacement at temperature T, so the $L_0 + \triangle L(T)$ represents the height of the sample at temperature T. Then it is relatively easy to derive the expression of densification rate:

$$\dot{\varepsilon}^s(T) = \frac{\dot{D}(T)}{D(T)} = \frac{-\Delta \dot{L}(T)}{20[L_O + \Delta L(T)]} \qquad (15)$$

where the coefficient 1/20 (3/60) is a result of the conversion to SI units, since the TMA counts time in minutes instead of seconds.

Fig.14 shows the representative densification rate-relative density curves observed in the alumina powder mixtures. Because of the similarity of the curves for 1) 10%-30% TMDAR powder mixtures, 2) 60%-90% TMDAR powder mixtures, only six densification curves including 0% and 100% TMDAR powders are shown to enhance the clarity of the plots.

As shown in Fig.14, increasing the proportion of TMDAR enhances both the green density and the final density of the samples. With the exception of the pure CR-15 sample, all of the specimens are nearly fully-sintered (D > 95%). Due to the high sintering capability of TMDAR, the samples containing a higher proportion TMDAR have higher fully-sintered densities.
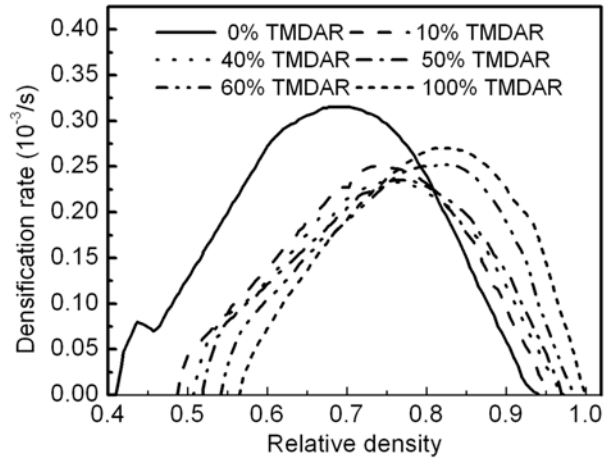

Fig.14 Densification rate as a function of relative density for TMDAR+CR-15 alumina powder mixtures. [18]

In the densification rate–relative density curve, one point of critical importance is the maximum densification rate point. Prior to reaching this point, there is no grain growth and the pores among the grains are parts of interconnected networks. These networks begin to collapse into isolated pores after the powder compact reaches its maximum densification rate, and rapid grain growth begins to occur [21]. From Fig. 4.8, the maximum densification rate for the alumina powder mixtures occurs within the relative density range of 70-84%, consistent with the results of Lance et al. [20] and Lange [22]. Another point of interest is that the increase in the proportion of TMDAR also increases the relative density at which the maximum densification rate occurs. This change is also a result of the increased green density of the samples caused by increased TMDAR proportion.

The ascending and descending parts of a densification curve are the segments before and after the maximum densification point, respectively. Fig. 14 shows that the powder mixtures with higher CR-15 proportions have higher densification rates in the ascending section and lower rates in the descending section of the curve. Ting et al. [21] concluded by theoretical calculation that "*Prior to the occurrence of grain growth, a maximum densification rate exists as the starting particle size distribution width increases, … During grain growth, the model predicts decreasing densification rate with increasing starting particle size distribution width.*" Our experimental observations match this conclusion since the increase in the proportion of CR-15 increases the particle size distribution width.

Depending on the powder mixture system, the ascending section for the densification

rate-relative density curves can be closely approximated by either one or two straight lines. The 100% TMDAR, agglomerate-free sample, exhibits a single linear segment with one slope. In contrast, systems containing CR-15 demonstrate two linear segments with distinct slopes. Lance et al. [20] obtained similar results by stating "*Agglomerates free alumina powder shows a single slope linear segment and powders with agglomerates show two linear segments.*"

Each powder mixture containing CR-15 features a plateau in the ascending portion of the curve in Fig.14. Even though the relative density and densification rate value are different for each powder mixture, the sintering temperature at which the plateau occurs is within the same temperature range (1150-1200°C). This plateau is a result of γ- to α-phase transition of alumina [23], since 10% γ-phase alumina is present in CR-15 (Table 2.1). TMDAR powder contains only α-phase alumina and no plateau in the pure TMDAR densification rate-relative density curve.

A plateau in descending section of a densification rate-relative density curve signifies the occurrence of abnormal grain growth [20]. It can be seen that no plateaus exist in that region for any curves in Fig. 4.8. This holds true even for a powder system with agglomerates (such as CR-15), which is known to cause abnormal grain growth.

Fig.15 shows the seven representative curves obtained for our zirconia powder system. The 10% and 20% CERAC-2003 systems as well as all the powder mixture systems between 50% and 80% CERAC-2003 exhibit very similar densification rate–relative density curves. The densification rate–relative density curve for each group is presented in Fig.15 as a single curve to allow for clarity.
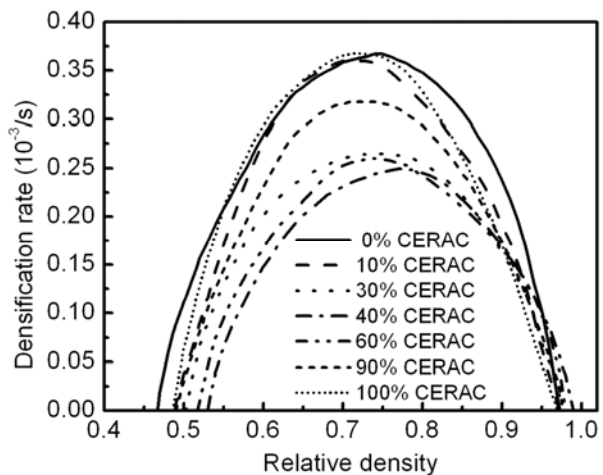

Fig.15 Densification rate as a function of relative density for TZ3YS+CERAC-2003 zirconia system. [18]

Fig. 15 shows that the green density of zirconia samples increases when the proportion of CERAC-2003 is between 0% and 40%, and begins to decrease beyond 40%. This is because the small TZ3YS particles fill in the interstitial spaces among the larger CERAC-2003 particles as well as the powders of the zirconia system feature very similar compactibility. The similarity in the sinteribilities of CERAC-2003 and TZ3YS results in a similar final density for various zirconia powder mixtures.

The maximum densification rate for each of our zirconia powder mixtures occurs within the relative density range of 74-82%. This result is consistent with the report of Trunec et al. [24]. The higher the green density of a powder mixture, the higher the relative density at which the maximum densification rate occurs. This is the same result found with our alumina powder mixtures. The densification rate in ascent and descent

part changes as the proportion of CERAC-2003, which also fit to the Ting's calculation [21].

3.3.2 Phenomenological constitutive models for sintering curves [18, 19]

In the last decades, a lot of research has been devoted to predict the densification kinetics of powder compaction [25-27]. Some of this research used the phenomenological model. The phenomenological model consists of fitting analytical expressions directly from the results of sintering experiments. Thus, it provides a constitutive equation describing as precisely as possible the real behavior of the material without regarding the physical meaning of its parameters.

An example of the phenomenological models is presented by Hsueh [27]:

$$\dot{\varepsilon}^s = \Omega(T)[D\infty(T) - D]^n \qquad (16)$$

where $D_\infty(T)$ is the theoretically possible full-sintered density at temperature T.

To fit the densification rate – relative density curves to Eq. (16), part-isothermal heating cycle sintering of samples is needed. The part-isothermal heating cycle sintering was first utilized by Dorn in 1957 [28]. The part-isothermal heating cycle used in ours study is shown in Fig.16.

Fig.17 shows the part-isothermal sintering test result for 100% TMDAR powder. Each "descending part" is from the isothermal sintering. If one extends each descending part and intersects the extension with the relative density axis, the intersection point gives the D_∞ for the temperature at which the isothermal sintering performed.

After obtaining a series of values of $D_\infty(T)$, the following steps are used to calculate the phenomenological constitutive model for each powder mixture in Figs. 4.8 and 4.9:

1. Taking the natural logarithm for the both sides of Eq. (16), a linear relationship can be found:
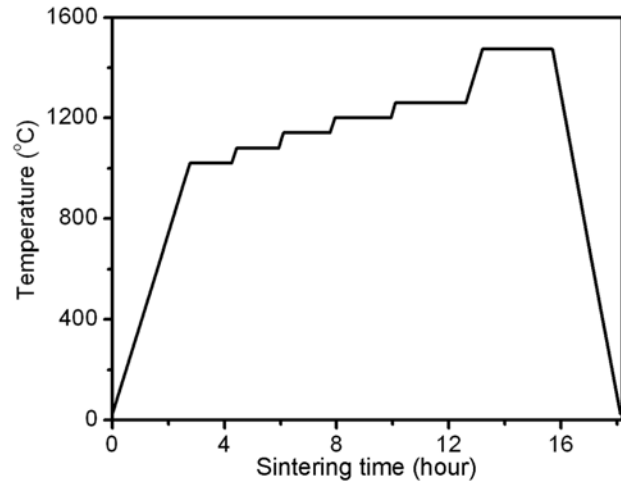

Fig.16 The part-isothermal ramp/soak sintering cycle used in this study to calculate the phenomenological constitutive models. [18]
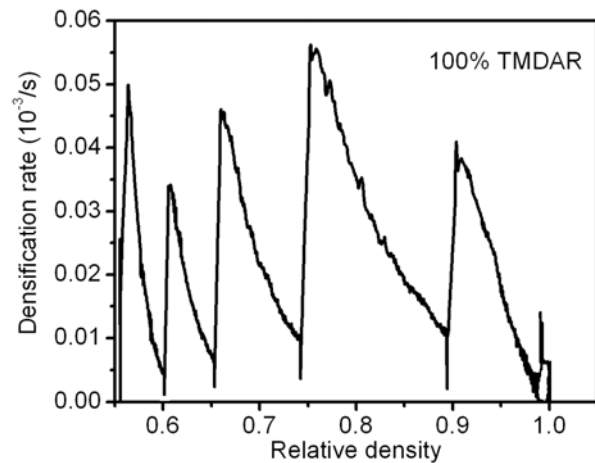

Fig.17 The densification rate – relative density relationship of the 100% TMDAR powder under the part-isothermal sintering path described in Fig. 16. [18]

17

$$\ln(\dot{\varepsilon}^s) = n\ln([D\infty(T) - D]) + \ln(\Omega(T)) \qquad (17)$$

2. Calculating $D\infty(T) - D$ for the relative density data of each isothermal sintering testing part and then taking the natural logarithm for the densification rate data and the $D\infty(T) - D$.

3. Using the linear function to fit the terms $\ln(\dot{\varepsilon}^s)$ and $\ln(D\infty(T) - D)$, a series of linear equations, each of which relates to a specific isothermal sintering temperature are obtained. Table 5 shows the linear equations calculated for pure TMDAR powder.

Table 5. The linear equations calculated for pure TMDAR powder [19]

Isothermal temperature (^oC)	Linear fitting equations
1020	$\ln(\dot{\varepsilon}^s) = 1.638\ln[0.6118 - D] - 1.6439$
1080	$\ln(\dot{\varepsilon}^s) = 1.652\ln[0.6802 - D] + 0.3165$
1140	$\ln(\dot{\varepsilon}^s) = 1.648\ln[0.792 - D] - 0.0657$
1200	$\ln(\dot{\varepsilon}^s) = 1.655\ln[0.973 - D] - 0.5173$
1260	$\ln(\dot{\varepsilon}^s) = 1.635\ln[0.995 - D] - 1.059$

4. The coefficients in front of $\ln(D\infty(T) - D)$ give the value of n in Eq.(17). From Table 5 we can see that the n value is nearly constant for a powder system under different temperature. The n for TMDAR is around 1.65.

5. The entries in Table 5 give a series value of $\ln(\Omega(T))$. Thus we can get a relationship between $\ln(\Omega(T))$ and temperature T, then use a polynomial to relate $\Omega(T)$ and T. For pure TMDAR, the $\Omega(T)$ can be expressed as:

$$\Omega(T) = -1.3799 \times 10^{-11}T^4 + 6.0705 \times 10^{-8}T^3$$
$$- 8.719 \times 10^{-5}T^2 + 0.037079T + 5.2474 \qquad (18)$$

6. A series $D\infty(T)$ values at different temperature T are also obtained. we can fit $D\infty(T)$ into a hyperbolic tangent function. For the pure TMDAR powder, the expression is:

$$D\infty(T) = \{0.2224\tanh[8.3785 \times 10^{-3}T - 9.4498]\} + 0.7776 \qquad (19)$$

7. Combining the result of steps 4-6, The final phenomenological constitutive model for each powder mixture is obtained.

The calculated phenomenological constitutive function for 100% TMDAR:

$$\dot{\varepsilon}^s = [-1.138\times10^{-11}(T)^4 + 0.503408\times10^{-7}(T)^3$$
$$-0.72765\times10^{-4}(T)^2 + 0.0319064(T) + 3.5792] \tag{20}$$
$$\times\{\{0.2224\tanh[8.3785\times10^{-3}(T+40)-9.4498]\}+0.7776-D\}^{1.5}$$

Fig. 18 shows the comparison of the experimental measurement and the calculated result by Eq. (20) for both the non-isothermal and part-isothermal heating cycles. The correlation between the calculated and experimental results remains very high for both two figures. The errors between the experimental data and the calculated results are less than $\pm6\%$.
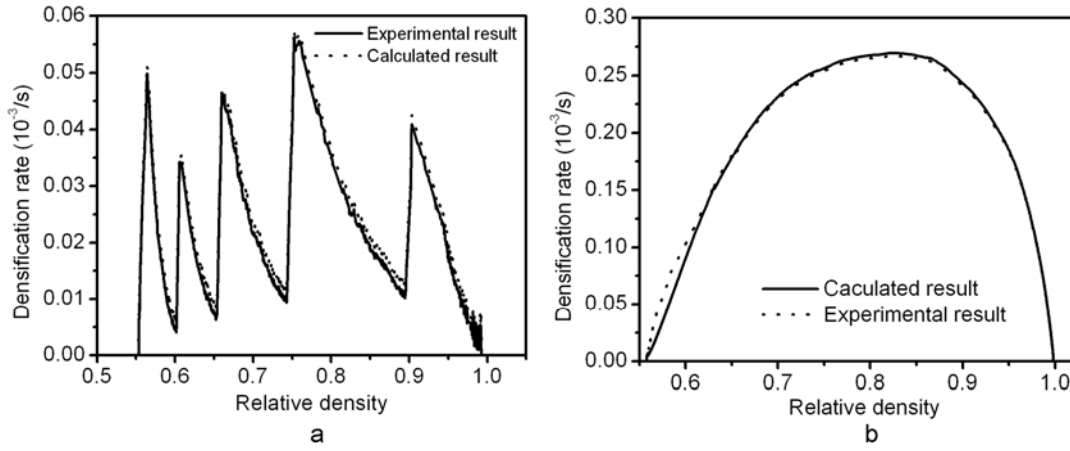
Fig.18 Comparison of the experimental and calculated results for 100% TMDAR under a) non-isothermal and b) part-isothermal heating circle [18]

The Hsueh's formula also can be applied to zirconia powder systems. The phenomenological constitutive equations for all zirconia powder mixtures are obtained. Fig. 19 shows the comparison of the experimental and the calculated results by Eq. (4.10) during the non-isothermal heating cycle. The errors between the experimental data and the calculated results are less than $\pm4\%$.

The equation to describe the sintering kinetics of pure TZ3YS is:

Fig.19 100% TZ3YS sintering [18]

$$\dot{\varepsilon}^s = [1.00465\times10^{-9}(T-150)^4 + 5.83063\times10^{-6}(T-150)^3$$
$$-1.26736\times10^{-2}(T-150)^2 + 12.2284(T-150) + 51384] \tag{21}$$
$$\times\{\{0.2409\tanh[9.5305\times10^{-3}(T)-12.259]\}+0.7444-D\}^{2.1}$$
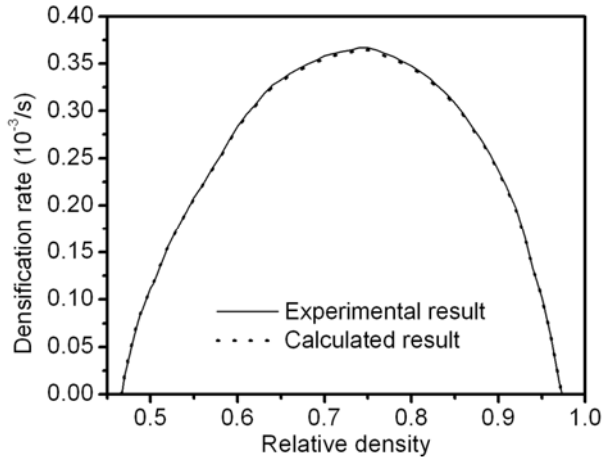
3.3.3 Application of Sintering kinetics curves on the fabrication of step-wise FGMs [19]

We successfully fabricated $ZrO_2/50ZrO_2+50Al_2O_3/Al_2O_3$ step-wise Functionally Graded Material (FGM), as shown in Fig.20. In the process, the powder selection for each layer is based on the sintering kinetics comparison.

To achieve the flatness in the FGM specimen (no significant camber), the sintering kinetics of each layer should be very similar. Comparing Fig. 14 and 15, one can find that most zirconia powder mixtures have higher densification rates than the alumina powder mixtures. In contrast to this trend, the curve of 40%CERAC-2003+ 60%TZ3YS (Powder *Z*), the zirconia powder system with the lowest densification rate, lies between 100%CR-15 and 90% CR-15+10%TMDAR curves.
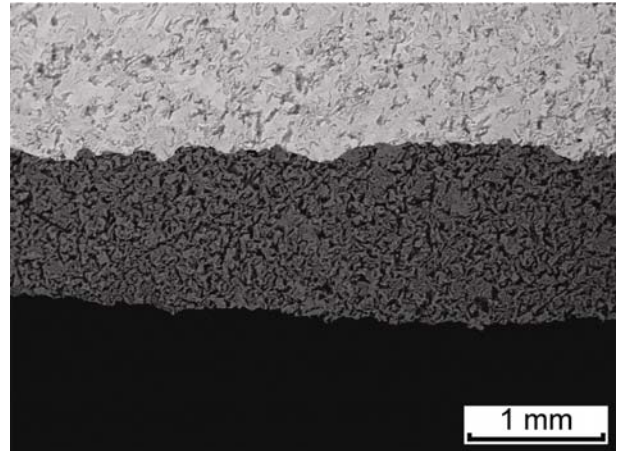

Fig.20. A representative Backscattered Electron image (BSEI) of the three-layered $Al_2O_3/Al_2O_3+ZrO_2/ZrO_2$ FGM [19].

Based on these two comparison results, several alumina powder mixtures were tested with the CR-15 powder varying between 100% and 85%. The TMA testing results revealed that the alumina powder mixtures containing 94% CR-15 and 6% TMDAR (Powder *A*) has very similar densification rate curve as Powder *Z* (Fig. 21). Also, sintered samples by Powder *A* and Powder *Z* had almost the same final diameter. These two powders were mixed in equal volume. The resulting powder mixture yielded a similar, not exactly the same, densification curve as Powders *A* and *Z*. This should be due to the change in the particle size distribution. However, considering the excellent sinterability of TMDAR, by making a small adjustment in the TMDAR proportion, the powder system with 46% CR-15, 4% TMDAR, and 20% CERAC-2003, 30% TZ3YS by volume (Powder *M*) shows a nearly same sintering behavior as Powder *A* and Powder *Z* (Fig. 21) as well as almost the same final diameter.
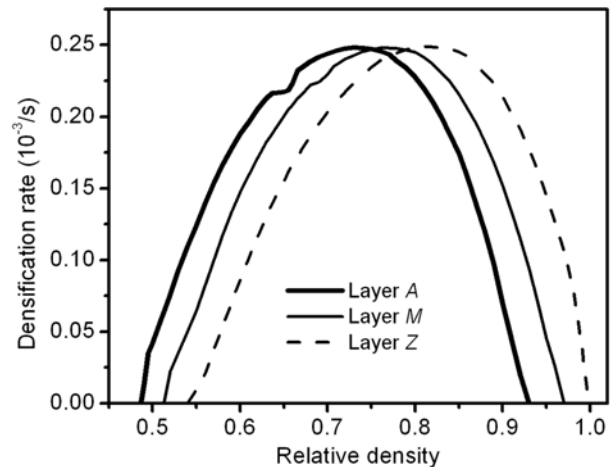

Fig.21. The densification rate-relative density curves of the three chosen powder mixtures (ramp rate: 10°C/min). [19]

The shape of the three curves in Fig. 21 is very similar. One obvious difference is located around $0.22 \cdot 10^{-3}$/s densification rate in the ascending portion. The corresponding sintering temperature range is 1150-1200°C. There is a plateau for layer *A* and a drop in slope for layer *M*, but there is no noticeable change for layer *Z* near this region. As

explained in Section 4.3.1, the change in densification rate for layers *A* and *M* is a result of γ- to α-phase transition of alumina [23] since 10% γ-phase alumina is present in CR-15. However, since layer *Z* does not contain CR-15, there is no plateau or abrupt slope change in its densification rate curve. The similarity among the sintering kinetics of the three powders results in no obvious difference in shrinkage rate and final diameter among layers during the co-sintering of a FGM sample. Therefore, the Powder *A*, *Z*. and *M* are the potential powders to achieve flat, crack-free three-layered Al_2O_3/ZrO_2 FGM samples.

3.3.4 CTEs measurement [29, 30]

By in situ reaction of WO_3 to ZrO_2, we fabricated various ZrW_2O_8/ZrO_2 composites, as listed in Table 6.

Table 6 The WO_3/ZrO_2 mass ratios of various green samples and the corresponding resultant ZrW_2O_8/ZrO_2 volume ratios in the sintered samples.

#	WO_3/ZrO_2 mass ratio in reactant powder	ZrW_2O_8/ZrO_2 volume ratios in the sintered sample	Final relative density
1	0.159:1	20:80	77%
2	0.264:1	30:70	79%
3	0.38:1	38.9:61.1	80%
4	0.593:1	51.5:48.5	82%
5	1.096:1	70:30	83%
6	2.307:1	90:10	84%

The temperature-dependent CTE value of each sintered sample was measured by the TMA, and shown in Fig. 22. As shown, both Samples 1 and 2 feature positive CTEs, Samples 4-6 exhibit negative CTEs, and the CTE of Sample 3 is nearly zero. Fig. 22 shows that the CTE-temperature curves of the composites feature a shape that is very similar to that of pure ZrW_2O_8. However, the peak caused by phase transition occurs at a lower temperature for the composites. This "peak shift" is possibly a result of phase transition from α-ZrW_2O_8 (low pressure phase) to γ-ZrW_2O_8 (high pressure phase) [31] due to the thermal stress induced by the CTE mismatch between ZrO_2 and ZrW_2O_8.
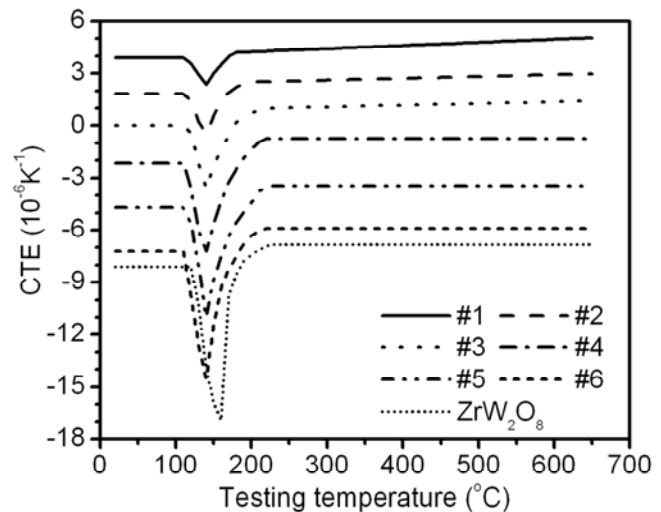
Fig.22 Temperature dependent CTEs of the various ZrW_2O_8/ZrO_2 composites [29].

3.3.5. Young's Modulus measure [29, 30]

The TMA unit offers a facility to measure Young's modulus of materials using the three-point bending method. After sintering and polishing, the samples used in Young's modulus testing are rectangular parallelepipeds (cuboids) with edge lengths 12.6mm, 4.2mm and 2.5mm. The temperature dependent Young's moduli of the fabricated composites listed in Table 6 as well as that of ZrW_2O_8 and ZrO_2 are shown in Fig. 23. Since the ZrO_2 in the composites is processed by the ramp/soak path with quenching step, the CERAC-2003 for Young's modulus testing was also partially sintered by the same ramp/soak

Fig.23 Young's modulus - temperature curves for composites as well as for ZrW_2O_8 and ZrO_2 [29].

path. Microcracks formed in the ZrO_2 samples due to the quenching process. The highest testing temperature was set as 650°C in order to avoid the decomposition of ZrW_2O_8. The room temperature Young's modulus of pure ZrW_2O_8 was found to be 4.31GPa, which nearly matches the value of 4.22GPa reported by Chen et al. [32]. However, these values quite different from the single crystal value of 88.3GPa reported by Drymiotis et al. [22]. Since the ZrO_2 sample was only partially sintered and contains microcracks, its Young's modulus is much lower than that of a fully-sintered sample (~200GPa) and it does not feature a large decrease from 100 to 400°C, which is typical for fully-sintered ZrO_2 [34]. the Young's moduli of the composites and the ZrW_2O_8 feature a value change around 160°C due to the α to β phase transition.

3.3.6. Verification of continuous gradient for ZrO_2-ZrW_2O_8 continuous FGMs [35,36]

A ZrO_2+WO_3 powder mixture and ZrO_2 powder were stacked, co-compacted and co-sintered in the processing steps commonly used for multi-layer materials. The observation of the cross-sectional microstructures indicated the sintered samples are continuous ZrW_2O_8/ZrO_2 Functionally Graded Materials (FGMs). At the same time, the measurement of the radial thermal expansion also provided evidence for the continuous gradient [35, 36]. The radial surface of each sample was polished to achieve two parallel planes. The radial thermal expansions of each sample
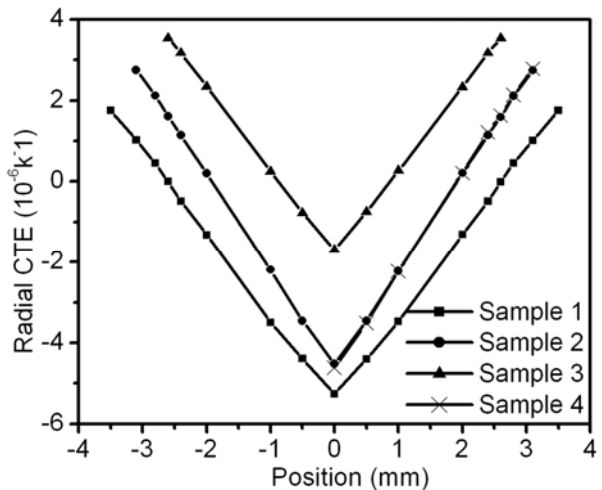

Fig.24 The radial thermal expansion-position relationship for sintering FGMs [35].

were then measured at several locations for each sample. It can be seen in Fig. 24 that the radial thermal expansions feature a continuously changing profile, providing additional evidence of a continuous gradient of the sintered FGMs.

Reference

[1] German R.M., (1994). *Powder metallurgy science*, 2nd ed., Metal powder industries federation, Princeton, pp. 15-24, 210-221, 242-262.

[2] Kieback B, Neubrand A and Riedel H. Processing techniques for functionally graded materials, Mater Sci Eng A, 2003;362:81-106

[3] Szabo D and Schneebeli M, Subsecond sintering of ice, Appl Phys Lett, 2007;90:151916

[4] http://www.mts.com/en/Material/Univ/Insight/index.asp

[5] L. Sun, B. Oguz, and P. Kwon, The effect of powder mixing on the compaction capabilities of ceramic powders, Powder Technology, under review.

[6] Westman A. E. R., and Hugill H. R. The packing of particles, J. Am. Ceram. Soc. 13 (1932), 767–779.

[7] McGeary R. K., Mechanical packing of spherical particles, Journal of American Ceramic Society 44(10) 1961 513-522

[8] Aydin I., Briscoe B. J. and Sanhturk K. Y. The internal form of compacted ceramic components: a comparison of a finite element modeling with experiment. Powder Technology, 89 (1996) 239-254

[9] Aydin, I., Briscoe, B., and Sanliturk, K. Y., Density distributions during the compaction of alumina powders: a comparison of a computational prediction with experiment, Computational Materials Science 1994 3 55-68.

[10] Aydin, I., Briscoe, B., and Sanliturk, K. Y., Dimensional variation of die-pressed ceramic green compacts: comparison of a finite element modeling with experiment, Journal of European Ceramic Society, 1997 17 1201-1212.

[11] Chen W. F. and Saleeb A. F. Constitutive Equations for engineering materials, Wiley, New York 1982, 155, 234-238

[12] D. H. Zeuch, J. M. Grazier, J. G. Arguello and K.G. Ewsuk, Mechenical properties and shear failure surfaces for two alumina powders in triaxial compression, J of Materials science, 2001, 36, 2911-2924

[13] Train D, Transmission of forces through a powder mass during the process of pelleting. Trans. Instn. Chem. Engrs, 1957, 35, 258-266

[14] Macleod, H. M. and Marshall, K., The determination of density distributions in ceramic compacts using autoradiography. Powder Technol., 1977, 16, 107-122

[15] Kwon, Y. S. and Kim K. T. Densification forming of alumina powder-effects of powder law creep and friction, J Eng. Mat. Techno. 1996, 118, 471-455.

[16] SETARAM instrumentation,User manual for Setaram

[17] O Gillia, D Bouvard, Phenomenological analysis of densification kinetics during sintering: application to WC–Co mixture, Mater Sci Eng A 279 (2000) 185-191.

[18] L. Sun, A. Sneller, and P. Kwon, Powder selection in cosintering multi-layered ceramic FGM

based on the densification kinetics curves, Journal of Composite Materials, 2009, 43, 469

[19] L. Sun, A. Sneller, and P. Kwon, Fabrication of alumina/zirconia functionally graded material: from optimization of processing parameters to phenomenological constitutive models, Materials Science and Engineering A, 2008, 488, 31.

[20] D. Lance, F. Valdivieso, P. Goeuriot, Correlatioon between desificaion rate and microstructural evolution for pure alpha alumina, J. Eur. Ceram. Soc. 24 (2004) 2749–2761.

[21] Ting J.M. and Lin R. Y., Effect of particle size distribution on sintering: Part I Modeling., J. Mater. Sci., 1994, 29, 1867-1872

[22] Lange, F. F. (1989). Powder Processing Science and Technology for Increased Reliability, J. Am. Ceram. Soc., 72(1): 3-15.

[23] Legros, C., Carry, C., Bowen, P. and Hofmann, H. (1999). Sintering of a Transition Alumina: Effects of Phase Transformation, Powder Characteristics and Thermal Cycle, J. Eur. Ceram. Soc., 19(11): 1967-1978.

[24] Trunec, M. and Maca, K. (2007). Compaction and Pressureless Sintering of Zirconia Nanoparticles, J.Am. Ceram.Soc., 90(9): 2735-2740.

[25] M. Missiaen, S. Roure, Acta Mater. 46 (1998) 3985-3993.

[26] J. Svoboda, H. Riedel, R. Gaebel, Acta Mater. 44 (1998) 3215-3226.

[27] Hsueh CH, Evans AG, Cannon RM and Brook RJ, Acta. Metall. 34 (1986) 927-936.

[28] J.E. Dorn, Creep and Recovery, 1st ed., Am. Soc. For Metals, Cleveland, 1957.

[29] L. Sun, and P. Kwon, ZrW2O8/ZrO2 composites by In-situ reaction of ZrO2+WO3: processing, properties and theoretical model predictions, Journal of Materials Research, under review.

[30] L. Sun, A. Sneller, and P. Kwon, ZrW2O8-containing composites with near-zero coefficient of thermal expansion fabricated by various methods: comparison and optimization, Composite Science and Technology, 2008, 68, 3425.

[31] Jorgensen J. D, Hu Z, Teslic S, Argyriou D. N, Short S, Evans J. S. O, Sleight A. W. Pressure-induced cubic-to-orthorhombic phase transition in ZrW_2O_8. Phys Rew B 1999;59(1):215-225.

[32] Chen J. C, Huang G. C, Hu C, Weng J. P. Synthesis of negative-thermal-expansion ZrW_2O_8 substrates. Scripta Mater 2003;49(3):261-266.

[33] DryMiotis F. R, Ledbetter H, Betts J. B, Kimura T, Lashley J. C, Migliori A, Ramirez A. P, Kowach G. R, Van Duijn J. Monocrystal elastic constants of the negative-thermal-expansion compound Zirconium Tungstate (ZrW_2O_8). Phys Rev Lett 2004;93(2):025502.

[34] Adams J. W, Ruh R. Mazdiyasni K. S. Young's modulus, flexural strength and fracure of yttria-stailized zirconia versus temperature. J Am Ceram Soc 1997;80(4):903-908.

[35] L. Sun, A. Sneller, and P. Kwon, ZrW2O8-ZrO2 continuous functionally graded materials: processing and the influence of soaking duration on microstructures, Composite Science and Technology, under review.

[36] B. Oguz, L. Sun, and P. Kwon, Finite element design and material fabrication of a self-cooling thermal protection system, Smart Materials and Structures, under review.